Journal of Manufacturing Processes xxx (xxxx) 1–16

Contents lists available at ScienceDirect

Journal of Manufacturing Processes

journal homepage: www.elsevier.com/locate/manpro

Understanding roughness parameters in ultra-thin L-PBF walls: A model-based investigation of surface defects

Olivier Poncelet [a, *], Camille van der Rest [a], Aude Simar [a, b]

[a] UCLouvain, Institute of Mechanics, Materials, and Civil Engineering (IMMC), IMAP, Place Sainte Barbe, 2, 1348, Louvain-la-Neuve, Belgium
[b] Wel Research Institute, Wavre, Belgium

ARTICLE INFO

Keywords:
Roughness
L-PBF
Modeling

ABSTRACT

Surface roughness remains a major concern in laser powder bed fusion (L-PBF), particularly in the context of thin-walled components where dimensional accuracy and fatigue performance are highly sensitive to surface defects. Although track energy density (TED) is known to influence surface quality, the underlying mechanisms remain poorly understood. In this work, a simplified geometry-based model is developed to explore the contribution of melt-pool geometry and sintered powder particles to surface roughness. The model relies on idealized stacked melt-pool shapes and randomly distributed surface particles, and is calibrated using experimental observations from L-PBF samples processed at different TED values. While the arithmetic average roughness (R_a) is commonly used to assess surface quality, this study emphasizes the relevance of additional parameters – R_p, R_v, R_{sk}, and R_{ku} – to better capture the morphological nature and statistical distribution of surface defects. Importantly, the results show that surface-adhered powder particles play a dominant role in shaping roughness, particularly at lower TED values. The model successfully reproduces experimental roughness trends and provides insight into the origin of surface features. These results demonstrate how different roughness parameters reflect specific surface morphologies and provide a framework for interpreting surface roughness beyond R_a in additive manufacturing.

1. Introduction

A major issue in laser powder bed fusion (L-PBF) additive manufacturing (AM) processes is the as-built surface roughness, which can reach very high values, with arithmetic roughness R_a exceeding 20 μm depending on the process parameters [1]. Surface roughness is known to be one of the main crack initiation origins under fatigue loading [2–9], which is a major concern in aerospace and automotive applications [10]. Indeed, the presence of valleys act as stress concentrators and promote early initiation of fatigue cracks [11,12]. It also tends to increase part inaccuracy [13,14], especially for very thin structures such as heat exchangers and lattices [15,16]. Surface roughness of L-PBF parts has thus been extensively studied, in particular for the main aerospace alloys processed by L-PBF, such as AlSi10Mg [1,9,13,17–19], Ti6Al4V [20], stainless steel 316L [21–23] and nickel-based superalloys [24–26]. Across these studies, a common approach to improve surface quality in L-PBF is to separate contour and core scan strategies and apply a higher track energy density (TED) to the contour regions. In most of these studies, R_a or its surface equivalent S_a are the surface amplitude parameters used [27]. Most of these studies rely on empirical approaches in which process parameters such as laser power, scan speed, layer thickness or scanning strategy are experimentally varied in order to minimize the arithmetic roughness R_a. While these works successfully identify processing windows leading to lower surface roughness, they generally provide limited insight into the underlying mechanisms governing surface morphology and how other roughness parameters evolve in response to these process variations. As a result, the evolution and physical interpretation of additional roughness descriptors such as R_p (peaks), R_v (valleys), R_{sk} (skewness) and R_{ku} (kurtosis) remain rarely discussed in the context of L-PBF surfaces.

R_a only provides information about the mean surface height and therefore cannot fully describe the morphology of the surface profile or the nature of the surface defects generated during the process. Parameters such as R_{sk} and R_{ku}, which are widely used in conventional surface metrology [28–30], provide complementary information on the asymmetry and statistical distribution of surface heights. These descriptors therefore help to distinguish between surfaces dominated by peaks, valleys, or isolated surface features. Such information is particularly relevant for L-PBF surfaces, which typically exhibit complex morphologies resulting from the layer-by-layer nature of the

* Corresponding author.

https://doi.org/10.1016/j.jmapro.2026.03.059
Received 8 August 2025; Received in revised form 13 March 2026; Accepted 25 March 2026
1526-6125/© 20XX

process and the presence of partially sintered powder particles. These surface features may influence the functional behaviour of components, for instance by promoting stress concentrations at surface valleys, affecting contact conditions, or modifying fluid–surface interactions in heat exchangers. Surface roughness also mainly affects how a component interacts with its environment and how it is used in practice. For instance, roughness may influence stress concentrations at the surface, fluid flow behaviour, contact conditions, or accessibility for post-processing. This aspect is particularly relevant for LPBF components, which are often designed as complex geometries such as internal channels, lattice structures or heat exchangers, where machining or surface finishing may be difficult or impossible. In such cases, the functional behaviour of the component can depend strongly on the statistical characteristics of the surface profile. The purpose of this work is to better interpret how different roughness parameters relate to the geometrical characteristics of LPBF-generated surfaces.

In order to address this issue and provide a better understanding of how standard surface amplitude parameters measured on L-PBF parts evolve with process parameters and surface features, a geometrical model validated against experimental measurements has been developed in the present work. The objective is to establish a direct link between measurable roughness parameters and the underlying surface morphology generated during the L-PBF process.

Roughness of L-PBF samples is a topographical measurement of the solidified melt-pool on the sides of the samples and is thus very sensitive to melt-pool morphology [1,9]. Fig. 1 presents a cross-section of one single wall track (SWT, stacked melt-pool wall) made of AlSi10Mg and illustrates the main contributions to roughness. A background roughness is expected due to the stratification (layer by layer process) which is inherent to the L-PBF process, leading to the so-called "staircase effect" when the building angle is larger than 0° [17,31]. This background roughness strongly depends on melt-pool instabilities and melt-pool size. On one hand, balling phenomenon (too low input energy) can induce large melt-pool size fluctuations (Fig. 1) [32–34], increasing the impact of the stratification. On the other hand, keyholing conditions [35,36] (too high input energy) can induce very large melt-pools thus limiting the stratification but leading to porosities [1]. Process parameters are generally chosen in a process window ensuring stable melt-pools with limited porosities [37,38]. Stratification will then contribute to roughness through the radius of curvature of the solidified melt- pools and will then depend on the material, on the TED and on the thickness of the layers selected for L-PBF manufacturing [24]. Roughness can also be increased due to the sintering of powder particles on the sample surfaces occurring during the manufacturing (Fig. 1). Spatters can also impact the roughness but are less prone to appear on vertical surfaces [39]. There are thus mostly two kinds of contribution increasing the roughness: the stratification and the sintered powder. Roughness due to stratification will be referred as primary roughness while roughness due to sintered powder particles will be referred as secondary roughness.

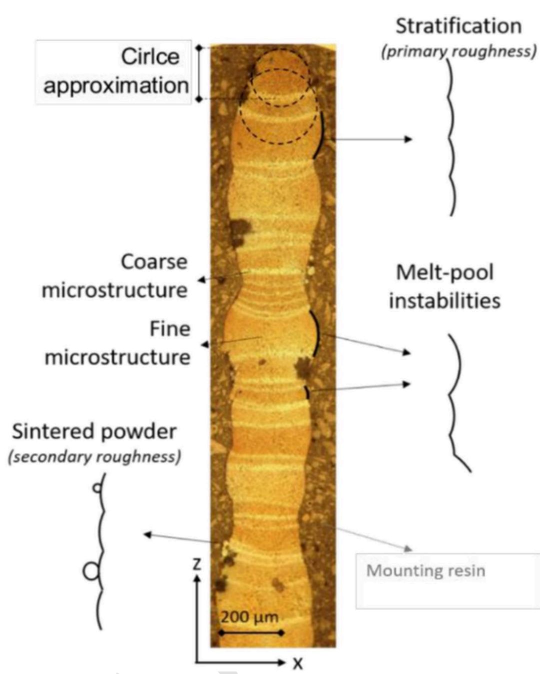

Fig. 1. Optical microscopy image of AlSi10Mg SWT cross-section after polishing and chemical etching, showing factors contributing to the roughness (stratification and sintered powder). Balling conditions here induce a large melt-pool size discrepancy, increasing the roughness, whereas the layer thickness is constant (30 µm). The whitish narrow bands are the coarse microstructure zones, corresponding to the bottom of each melt-pool. Yellowish parts are the fine microstructure zones, corresponding to the core of each melt-pool. Z is the building direction.

2. Materials and methods

2.1. Theoretical background about roughness

The most relevant surface texture parameters used in this work are detailed hereafter (from ISO 4287 standard), where l is the evaluation length (also noted ln, i.e. the profile length) and *Z(x)* is the profile height centered around its mean line:

R_a: roughness average, the arithmetic average of the absolute values of the profiles.

$$R_a = \frac{1}{l}\int_0^l |Z(x)|\, dx \tag{1}$$

R_p: the maximum profile peak height, which is the mean of the maximum distance between the highest profile point and the mean line, computed on five sampling lengths (lr), where $5\text{lr} = \text{ln}$.

R_v: the maximum profile valley depth, which is the mean of the maximum distance between the lowest profile point and the mean line, computed on five sampling lengths.

R_q: the root means square roughness average, defined as

$$R_q = \left[\frac{1}{l}\int_0^l Z(x)^2 dx\right]^{\frac{1}{2}} \tag{2}$$

R_{sk}: the profile skewness, a measure of the asymmetry of the profile about the mean line, defined as

$$R_{sk} = \frac{1}{l}\frac{1}{R_q^3}\int_0^l Z(x)^3 dx \tag{3}$$

R_{ku}: the profile kurtosis, a measure of the distribution flattening of the profile, defined as

$$R_{ku} = \frac{1}{l}\frac{1}{R_q^4}\int_0^l Z(x)^4 dx \tag{4}$$

ADF: the profile Amplitude Distribution Function.

R_a, R_p, and R_v are related to the surface height elevation. R_p and R_v give the maximum peak height and valley depth of a profile. R_p (R_v) increases proportionally to the height (depth) of the peak (valley). $R_p > R_v$ implies a peak-type profile, $R_p < R_v$ indicates a valley-type profile and $R_p = R_v$ means an equal number of peaks and valleys. R_q is the standard deviation of the profile height around the mean line and is used to normalize the skewness and the kurtosis. R_{sk} and R_{ku} are linked to the shape of the amplitude distribution function (described in the next paragraph and illustrated in Fig. 2). R_{sk} indicates whether the roughness is dominated by peaks ($R_{sk} > 0$) or by valleys ($R_{sk} < 0$). R_{ku} quantifies deviations in surface roughness compared to a Gaussian distribution, which serves as a reference with a kurtosis of 3—a fundamental statistical property. Note that R_{sk} of a Gaussian distribution is 0. A surface with $R_{ku} = 3$ follows a normal height distribution, while $R_{ku} < 3$ indicates a more uniform, plateau-like topography, and $R_{ku} > 3$ signifies pronounced peaks and valleys. In practice, natural roughness rarely exhibits $R_{ku} \leq 2$, as this would require an exceptionally uniform distribution of heights, typically observed in finely machined or polished surfaces. R_{ku} can typically reveal if there is an anomaly in the surface height distribution ($R_{ku} \gg 3$).

The amplitude distribution function (ADF) gives the probability to find material at a given height of a specific profile and can be represented as a curve or as a bar plot. ADF is computed by taking the derivative of the material ratio curve (Abbott-firestone curve), which is the evolution of the bearing length ratio ($R_{mr(c)}$) as a function of a cut level c(Fig. 2). As illustrated in Fig. 2, c is the distance, from the maximum profile height and toward the minimum profile height, at which a bearing length is computed. The bearing length is the total length of material exceeding the profile height of a specific cut level ($l_{c1} + l_{c2}$ in Fig. 2). R_{sk} and R_{ku} also give information about the shape of the ADF and thus indicate how the material is distributed over the profile height. The skewness indicates how asymmetric the ADF is around the profile mean line. A positive (negative) R_{sk} means that most of the material lies below (above) the profile mean line, indicating a peak-type (valley-type) profile.

The kurtosis indicates how sharp or broad the width of the ADF is and indicates if the material is homogeneously distributed over the profile height ($R_{ku} < 3$) or not ($R_{ku} > 3$). All the parameters selected in this work (R_a, R_p, R_v, R_{sk}, R_{ku} and ADF) are surface height parameters and give information about profile height deviation.

2.2. Manufacturing of the SWT samples

AlSi10Mg Single wall tracks (SWT) were processed by L-PBF with a ProX® DMP 200 (3D Systems Inc.) machine with a laser operating at 1075 nm, a spot size of 70 µm and a 275 W maximum power (Pmax). SWT consist of 15 mm-high and 10 mm-wide walls, formed by stacked melt pools, resulting in a thickness corresponding to a single melt pool. Gas atomized AlSi10Mg spherical powder was provided by TLS Technik, with D10, 50, and 90 values of 11, 26, and 46 µm, respectively. The layer thickness (L) was fixed at 30 µm for all samples. The building plate, made of Al5Mg, was a 141 mm × 141 mm × 15 mm square and was not heated during the L-PBF process, remaining around room temperature. L-PBF was conducted under an argon atmosphere, maintaining a residual oxygen concentration below 500 ppm. Samples were built directly on the substrate without support structures, and no post-processing treatments were applied. The track energy density (TED), defined as the laser power divided by the scan speed, was varied between 250 and 700 J/m. SWT were processed at a fixed scan speed of 400 mm/s, with laser power ranging from 40% to 100% of Pmax. Each layer was produced using a single laser track corresponding to a single line exposure. The scanning direction alternated between layers following a back-and-forth strategy.

2.3. Roughness analysis

Roughness analyses were conducted using a Keyence VHX-7000 digital microscope in accordance with the EN ISO 13565-1 standard. Each sample was examined at a magnification of ×200. A traverse length of 15 mm was then measured on each sample to calculate the roughness parameters. The traverse length was taken following the *Z*-direction (see Fig. 1) perpendicular to the melt pools and divided into five sampling lengths of 2.5 mm each, with a start-up and run-off length of half the long wavelength cut-off (λc/2). The cut-off for short wavelengths (λs) was set to 8 µm, and for long wavelengths (λc) at 2.5 mm. Subsequently, the following roughness parameters were computed: R_a (arithmetic roughness), R_p (maximum peak height), R_v (maximum valley depth), R_{sk} (skewness), and R_{ku} (kurtosis) (refer to Section 2.1). Each sample was measured 4 time on four different traverse lengths.

2.4. Geometrical characterization of SWT samples

All the samples were then cut in half, mounted and polished down to 1 µm. A chemical etching was performed with a Keller's reagent to reveal the microstructure. The melt-pool size and the real layer thickness (*L*) of each sample were measured with a Keyence VHX-7000 digital microscope. For SWT samples, the melt-pool size is the sample thickness and is equal to 2R (R = radius). *L* is considered as the distance between two successive melt-pools in the build direction and is measured as the distance between two heat-affected zone (HAZ). For each sample, 15 data points were recorded for both the melt-pool size and *L* with a ×300 magnification. In the following, measured thicknesses will be compared to Rosenthal equation [40]:

$$T(\mathrm{R}) = T_0 + \frac{1}{\mathrm{R}}\frac{Q}{2\pi k}\exp\left[-v\left(\frac{\mathrm{R}+\tilde{x}}{2\alpha}\right)\right] \quad (5)$$

where $T_0 = 308.15$ K is the initial temperature (building plate), $Q = P_l A$ [W] the input power where P_l is the laser power and $A = 0.32$ the material absorptivity, $k = 110$ W/mK the thermal conductivity, v [m/s] the laser scanning speed, $\alpha = k/\rho c_p$ [m^2/s] the thermal diffusivity in which $\rho = 2670$ kg/m^3 is the material density and $c_p = 915$ J/kg K the specific heat, $\tilde{x} = x + vt$ is the laser scan direction (v = laser scan speed and t the time), and R is the distance from the power source defined as $R = \sqrt{\tilde{x}^2 + y^2 + z^2}$. Materials properties are extracted from [41] but may vary depending on the sources. The input power and the laser scan speed are given in the manufacturing section. This equation gives

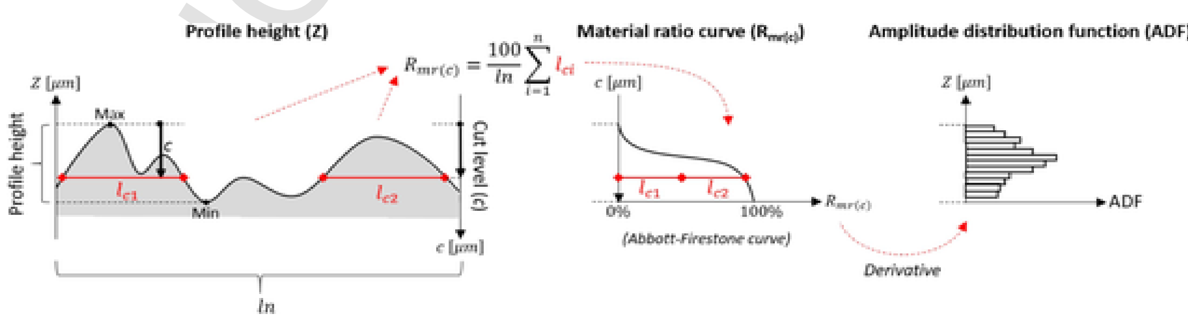

Fig. 2. Schematic showing how the amplitude distribution function (ADF) is generated. The mean line is the mean of the profile height. The cut level ranges from the maximum profile height to the minimum profile height. The profile height Z ranges from the minimum profile height to the maximum profile height.

the shape and size of a melt-pool (at $T(\mathrm{R}) = T_f = 849$ K, the melting point of the material) depending on input energy and material properties given a few hypotheses [39]: heat flow is steady-state, heat source has a point-like shape, no heat is associated to melting, the thermal properties are constant, no heat losses from the surface and no convection in the melt-pool. This simplified model, despite its restrictive assumptions, is still well in agreement with experimental observations and is often used in geometrical models of the L-PBF process [41–44]. It should be noted that the Rosenthal solution was originally derived for a moving heat source in a semi-infinite bulk medium. In the case of thin-walled structures, lateral heat dissipation is significantly reduced due to the limited surrounding material, which can lead to larger melt pools than those predicted by the classical formulation. Nevertheless, the Rosenthal model is retained to emphasize that melt-pool dimensions in thin-walled geometries may significantly differ from those typically observed in bulk LPBF structures. Particle size and spatial density were estimated from SEM observations of adhered powder particles on LPBF side surfaces.

3. Model description

During the L-PBF process of single-wall tracks or the contours of thin walls, the latest solidified melt-pool cross-section (i.e., the top melt-pool) has a shape that can be approximated by a circle (Fig. 1). During the processing of the next layer, the previous melt-pool is partially re-melted, leaving a new half-circle melt-pool on top of it. The remaining side-part of the re-melted previous layer becomes part of the profile. This process is repeated over and over, leading to a stratification effect. The model described here is developed based on these observations.

Fig. 3 presents the model, which aims to study the effect of stratification on surface roughness. Profiles are generated by stacking circles, as illustrated in Fig. 1, mimicking the approximate stacking of melt-pools. While in reality, melt-pools are not perfectly circular, the remaining side-part that contributes to surface roughness can still be reasonably approximated by a small circular arc. This assumption, though slightly different from the actual geometry, captures the essential roughness formation mechanism. Embedded circles lead to roughness profiles similar to those observed experimentally. The spacing between each circle corresponds to the layer thickness of the L-PBF process, and the circle radius corresponds to the melt-pool radius. To account for melt-pool instabilities and experimental uncertainties, stochastic variations are introduced in the layer thickness and melt-pool radius for each circle. Two situations can thus be studied: “ideal cases” where errors = 0, and “realistic cases” where errors ≠ 0.

Sintered particles are modeled as small circles added to the profiles, as illustrated in Fig. 3. Most L-PBF powders used today are produced by atomization and are nearly perfectly spherical. The effect of particle size (diameter) and density (number of particles per unit length, expressed in millimeters) on the profile can thus be studied. Sintered particles are spaced at regular intervals, with minimal penetration into the profile to represent a worst-case scenario. The effect of powder can be analyzed in both ideal and realistic cases.

The model produces thus profiles, which are analyzed, as the experimental data, with the ISO 4287 standard. The most relevant surface texture parameters ($\mathrm{R_a}$, $\mathrm{R_p}$, $\mathrm{R_v}$, $\mathrm{R_{sk}}$, $\mathrm{R_{ku}}$, and ADF), described in Section 1, were selected to characterize roughness. The length of the generated profiles was chosen according to the ISO 21920 standard. The traverse length is fixed at 15 mm (lt), and the evaluation length (ln) is fixed at 12.5 mm, corresponding to approximately 400 melt-pools or stacked circles. This evaluation length is divided into five segments, leading to a sampling length (lr) of 2.5 mm.

This model allows the study of process instabilities, such as melt-pool size and layer thickness variations, and their effect on surface roughness. Since the melt-pool size is directly linked to TED, the model can also be used to investigate the impact of TED on roughness. Additionally, the influence of sintered powder characteristics (size and density) can be analyzed. In total, six parameters are considered:

- R: melt-pool radius
- ΔR: melt-pool radius variation
- L: layer thickness
- ΔL: layer thickness variation
- Sintered particle density
- Sintered particle size

The model was implemented in MATLAB® (version R2021a, The MathWorks, Natick, MA, USA). First, the center position of each circle representing the melt-pool cross-section is computed along the build direction. The horizontal position of the *i*th melt-pool center is defined as

$$x_i = (i-1)\,\mathrm{L_i} \tag{6}$$

where $\mathrm{L_i}$ corresponds to the layer thickness. $\mathrm{L_i}$ is equals to L if the layer thickness is constant. Then, for each center position, a circular melt-pool profile is generated using the equation of a circle of center x_i and radius $\mathrm{R_i}$ where $\mathrm{R_i}$ represents the melt-pool radius associated with the *i*th melt-pool. The upper half of the circle is considered, since it represents the material surface after solidification:

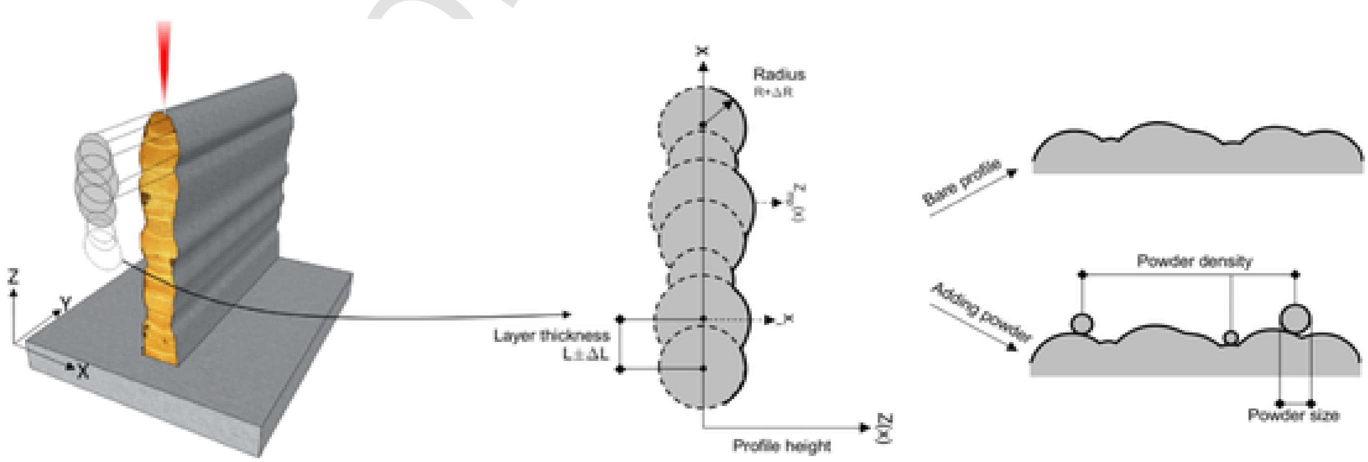

Fig. 3. Schematic representation of the roughness model. Stacked melt-pools are modeled by stacking circles. The layer thickness is the distance between the center of two circles and the radius of circles represent the melt-pool size.

$$z\left(x_i\right) = \sqrt{R_i^2 - \left(x - x_i\right)^2} \tag{7}$$

To introduce random variability in the model, perturbation terms were generated using the MATLAB function *rand* providing a random number between 0 and 1, following the expressions

$$\mathrm{L_i} = \mathrm{L} + \Delta\mathrm{L}\left(1 - 2 \bullet rand\right) \tag{8}$$

$$\mathrm{R_i} = \mathrm{R} + \Delta\mathrm{R}\left(1 - 2 \bullet rand\right) \tag{9}$$

Where L and R are the nominal thickness layer and radius. This ensures a uniformly distributed random variation within the ranges [−ΔL, ΔL] and [−ΔR, ΔR] around the nominal values of R and L, respectively. The overall surface profile is then constructed by taking the upper envelope of all melt-pool sections (Fig. 3):

$$Z_{mp}(x) = \max_i \left(z\left(x_i\right)\right) \tag{10}$$

In the following, the subscript p refers to quantities associated with adhered powder particles. Let l be the profile length and ρ_p the prescribed particle surface density (particles per mm). The total number of particles N_p introduced along the profile is defined as

$$N_p = \rho_p l \tag{11}$$

Assuming a regular spatial distribution along the profile, the horizontal spacing between two consecutive particles is given by

$$\Delta x_p = \frac{l}{N_p - 1} \tag{12}$$

The horizontal position of the center of the jth particle is therefore

$$x_{p,\ j} = (j - 1)\,\Delta x_p \quad j = 1, \cdots, N_p \tag{13}$$

Each particle is assumed to rest on the local surface profile. If $r_{p,j}$ denotes the particle radius, the vertical position of the particle center is defined as

$$z_{p,j} = Z_{mp}\left(x_{p,j}\right) + r_{p,j} \tag{14}$$

Each adhered particle is then represented by a circle, whose equation is

$$Z_{p,j}(x) = z_{p,j} + \sqrt{r_{p,j}^2 - \left(x - x_{p,j}\right)^2} \qquad \left|x - x_{p,j}\right| \le r_{p,j} \tag{15}$$

Similarly to the melt-pool construction, the final surface profile Z(x) is defined as the upper envelope of all geometrical contributions, including both melt-pool geometries and adhered particles:

$$Z(x) = \max\left[Z_{mp}(x), Z_{p,j}(x)\right] \tag{16}$$

To validate this model, all these parameters were experimentally measured on manufactured samples. The obtained values were then used as inputs in the model to generate theoretical roughness parameters. These theoretical values were subsequently compared with the experimentally measured roughness parameters from the corresponding samples.

4. Model parameterization

To determine appropriate values for the six model parameters and validate the model, single-wall tracks (SWT) were fabricated (see Section 2) and experimentally characterized. The experimental measurements were used to constrain the model parameters so that the simulated profiles reproduce the characteristic profile heights and surface features observed in the SWT experiments. Fig. 4 presents all SWT cross-sections. The SWT thickness increases with TED, and a keyholing mode seems to appear at 481 J/m.

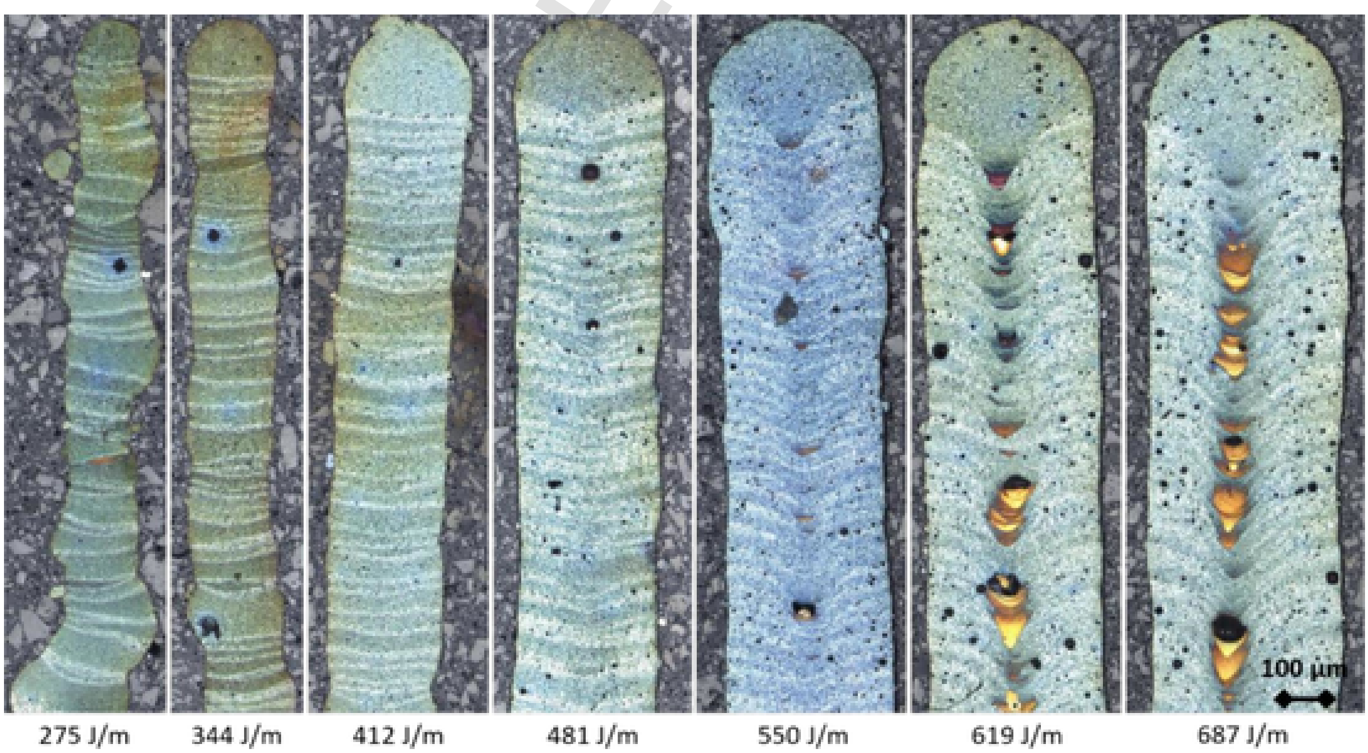

Fig. 4. Cross section of SWT made with different track energy density (TED).

Fig. 5 shows the measured melt pool size and layer thickness as a function of TED. Notably, Rosenthal's equation accurately predicts the melt pool size only at low TED values. However, this prediction can be improved by adjusting the absorptivity. The deviation observed in the measurements compared to Rosenthal's model corresponds to the transition between conduction and keyhole regimes. The latter induces higher absorptivity, thereby increasing the melt pool size, an effect that is not accounted for in Rosenthal's formulation. In addition, Rosenthal's model assumes heat conduction in a semi-infinite medium, whereas in the case of single wall tracks (SWT) the finite wall thickness limits heat dissipation and alters the thermal field. In other words, the reduction from an idealized infinite domain to a finite geometry is not captured by the analytical solution. Most of the melt pool width measurements exhibit a standard deviation between 10 and 20 μm.

The layer thickness, defined as the distance between two repetitive features (bottom of the melt pool in this case) along the build direction, is around 42 μm with a standard deviation of 12 μm for most samples (Fig. 5b). It increases slightly as TED decreases. The sudden increase observed below 412 J/m is attributed to melt pool instabilities, as illustrated in Fig. 4.

Characterizing the size and spatial density of adhered powder particles is more challenging than for the other geometrical features considered in this study. Both parameters are highly heterogeneous along the surface, as particle adhesion depends on the local surface morphology and on the process parameters (Fig. 6). As a result, the spatial distribution of particles is irregular and varies locally along the measured profiles.

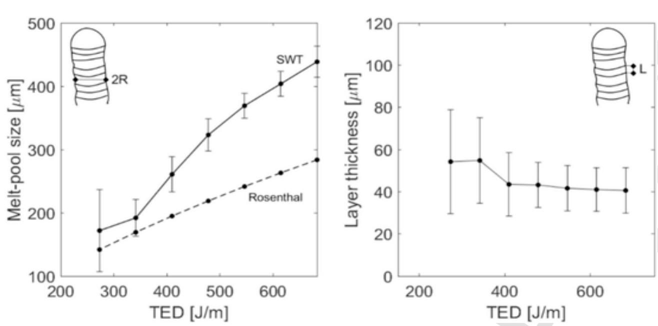

Fig. 5. (a) Melt-pool width, compared with Rosenthal's equation (dashed curve), and (b) layer thickness of SWT made with different TED.

To keep the geometrical model tractable and to limit the number of independent variables, this complexity was simplified in the simulations. Adhered particles were therefore represented using a single representative particle diameter and a constant spatial spacing along the surface profile. This approach allows the influence of particle size and particle density on the resulting roughness parameters to be isolated while keeping the model physically interpretable.

Nevertheless, in order to remain consistent with the actual surface morphology, a quantitative assessment was performed based on SEM observations to obtain realistic orders of magnitude for both particle size and particle density. The SEM images reveal that adhered particles typically range from a few micrometers to approximately 40 μm in diameter, which is consistent with the original powder size distribution used in this study (see Section 2.2). A slightly higher proportion of larger particles was qualitatively observed on samples processed at lower track energy densities (TED). In addition, particle density was roughly estimated by manually counting adhered particles along several surface segments of approximately 1 mm in the SEM images. These observations suggest a typical particle density between 3 and 7 particles/ml.

Within these experimentally observed bounds, the selected values were chosen so that the simulated profiles reproduce the overall roughness levels measured experimentally while remaining consistent with the particle sizes and densities observed in the SEM images. The values used in the simulations were therefore selected within this experimentally observed range: the particle density was set to 7 particles/mm for the 275 J/m sample and to 5 particles/mm for all higher TED conditions. Similarly, representative particle diameters were chosen to remain consistent with the sizes typically observed on the surface, leading to values of 30 μm for 275 J/m, 23 μm for 344 J/m, 13 μm for 412 J/m, and 11 μm for higher TED values. These values reflect the typical particle sizes and surface coverage observed on the studied samples rather than the exact characteristics of a specific profile.

While this approach introduces a limited degree of parameter adjustment, it allows the model to remain both interpretable and representative of the underlying process physics. Rather than reproducing individual measured profiles, the objective is to construct a generative and physically motivated model capable of reproducing the average surface characteristics observed across multiple samples. Using representative values for particle size and density is therefore consistent with the experimental procedure, which itself relies on averaged roughness measurements obtained from three profiles per condition.

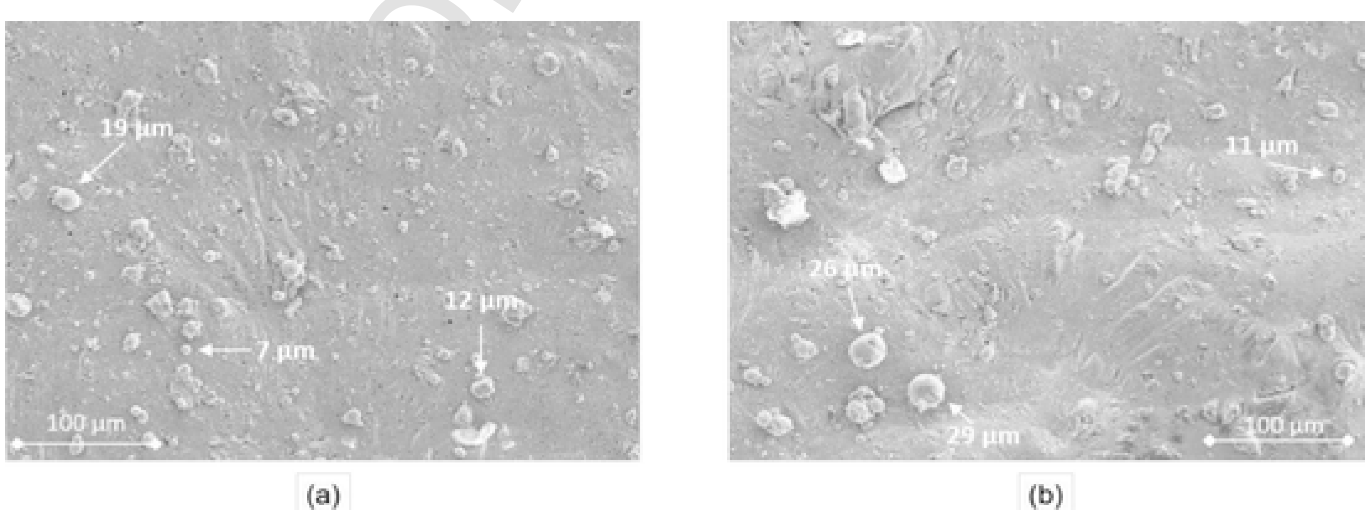

Fig. 6. SEM images of the side surface for (a) 481 J/m and (b) 344 J/m, illustrating the presence and typical size range of adhered powder particles.

The distribution of particles, coupled with melt-pool variability, reproduces realistic surface profiles while avoiding overfitting. Fig. 7 compares experimental measurements (minimum and maximum bounds of the experimental measurements are provided in grey) with theoretical predictions obtained using the above parameters. The model captures both the trend and the absolute values of all five roughness indicators. R_a decreases as TED increases and stabilizes at 550 J/m (Fig. 7a). Both R_p and R_v follow a similar trend (Fig. 7b), while R_{sk} and R_{ku} progressively shift toward (0;3), corresponding to a Gaussian-like distribution. Although the model simplifies several aspects of the L-PBF process, it successfully reflects the key characteristics of roughness evolution in ultra-thin walls.

5. Results

In the following section, the model is used to explore different scenarios. Fig. 8 presents several examples of profiles generated for the various studied cases. First, the model is applied to ideal conditions (Fig. 8a), meaning no perturbations are introduced in the melt-pool size (R) or the layer thickness (L). These conditions establish the lowest roughness level achievable solely due to stratification. “Ideal cases” also help isolate the primary effects of TED and layer thickness (Fig. 8a) on profile topography and, consequently, on roughness. Next, the model is used to assess the influence of sintered particles (Fig. 8b) on roughness parameters. By relying on “ideal cases,” the intrinsic effect of particle size and density can be isolated and analyzed. Finally, “realistic cases” are investigated. First, the effect of layer thickness variations (ΔL) is examined (Fig. 8c). Then, melt-pool instabilities are introduced by adding random fluctuations to the melt-pool radius (ΔR, Fig. 8d). The combined effect of sintered particles and process instabilities is also studied (Fig. 8e and f) to evaluate their impact on roughness parameters.

To assist in the interpretation of the simulated surface morphologies, the results are also represented using R_p–R_v and R_{sk}–R_{ku} parameter maps. These paired representations allow complementary aspects of the height distribution to be examined simultaneously: R_p and R_v reflect the relative contributions of peaks and valleys, while R_{sk} and R_{ku} describe the asymmetry and sharpness of the height distribution (occurrence of isolated peaks or deep valleys within the height distribution). Such combined representations are commonly used in surface characterization studies to highlight morphological trends that may be less apparent when considering each parameter independently.

However, interpreting R_{sk}–R_{ku} diagrams can be less straightforward, as the numerical values of these higher-order parameters are generally less intuitive than commonly used amplitude parameters such as R_a, R_p, or R_v. To facilitate their interpretation, the figures include a horizontal line at $R_{ku} = 3$ and a vertical line at $R_{sk} = 0$, corresponding to the reference case of a Gaussian height distribution. These reference lines provide a visual guide to assess how the simulated surface profiles deviate from, or progressively approach, a Gaussian distribution.

5.1. Ideal cases

5.1.1. Effect of TED and layer thickness

Studying ideal cases highlights that a background roughness will always persist in L-PBF due to the stratification induced by the melt-pool geometry. This defines the lowest theoretical roughness level achievable with this technique. While stratification may be barely visible to the naked eye when using small layer thicknesses [13], it remains relevant to characterize it.

Fig. 9 illustrates how roughness evolves with TED for two different layer thicknesses. The melt-pool size, which increases with TED, is derived from experimental data (Fig. 5). R_a clearly decreases as TED increases, meaning that a larger melt-pool size results in lower roughness. This effect is less pronounced for a 30 μm layer thickness than for a 90 μm layer thickness. Indeed, with a 30 μm-thick layer, the residual melt-pool curvature is minimal compared to a 90 μm-thick layer (Fig. 8a), limiting the impact of increasing melt-pool size. The R_a level achieved with $L = 30$ μm is particularly low (around 0.3 μm), representing the minimum R_a attainable under ideal L-PBF conditions for this layer thickness. This limit rises significantly with increasing layer thickness but remains relatively small, even in the worst-case scenario here (3.5 μm max at 275 J/m and $L = 90$ μm).

For both layer thicknesses, R_v consistently exceeds R_p and decreases with increasing TED. This indicates that the profiles are valley-type (with more material above the mean line) and that higher TED values lead to profile flattening. This is confirmed by a $R_{ku} < 3$, decreasing toward 2. R_{sk} further confirms that all profiles exhibit a valley-type morphology, as R_{sk} remains systematically negative. With R_{ku} values between 2 and 3, the amplitude distribution function (ADF) is flatter than a normal distribution. In this context, neither TED nor layer thickness significantly affects R_{sk} and R_{ku}. Examples of ADFs are provided in Fig. 10. The material distribution and ADF shapes are similar across the profiles analyzed here, which explains the limited impact of TED and layer thickness on R_{sk} and R_{ku}. ADF clearly shows that profile height values are homogeneously distributed over the whole profile height with an increasing distribution for the higher heights. This gives the combination of $R_{sk} < 0$ and $R_{ku} < 3$, characteristic of a smooth valley profile.

5.1.2. Effect of sintered particles

The intrinsic effect of sintered particles is analyzed at a fixed melt-pool size ($R = 160$ μm) and a fixed layer thickness ($L = 30$ μm). Fig. 11 illustrates how roughness evolves with varying sintered particle densities and sizes. The impact on R_a follows a clear trend: increasing the density of sintered powder raises R_a, and larger sintered particles further amplify this effect. While 10 μm particles have a limited influence,

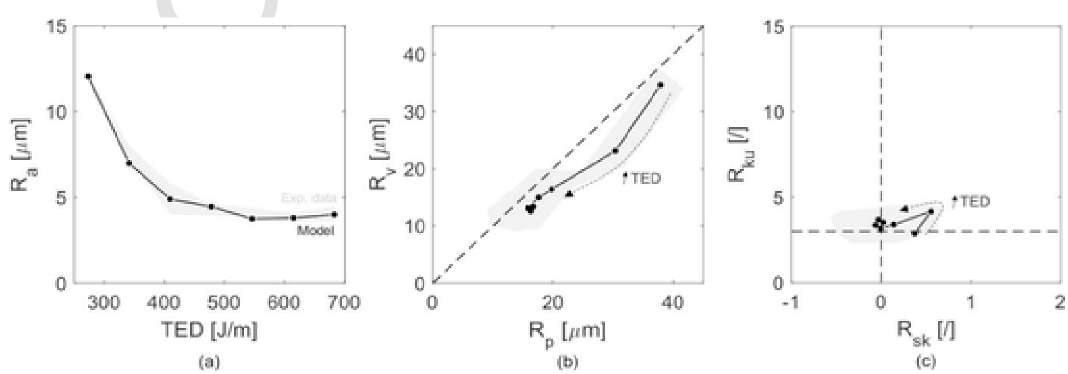

Fig. 7. Comparison between experimental measurement (grey surface) and model data (black curve).

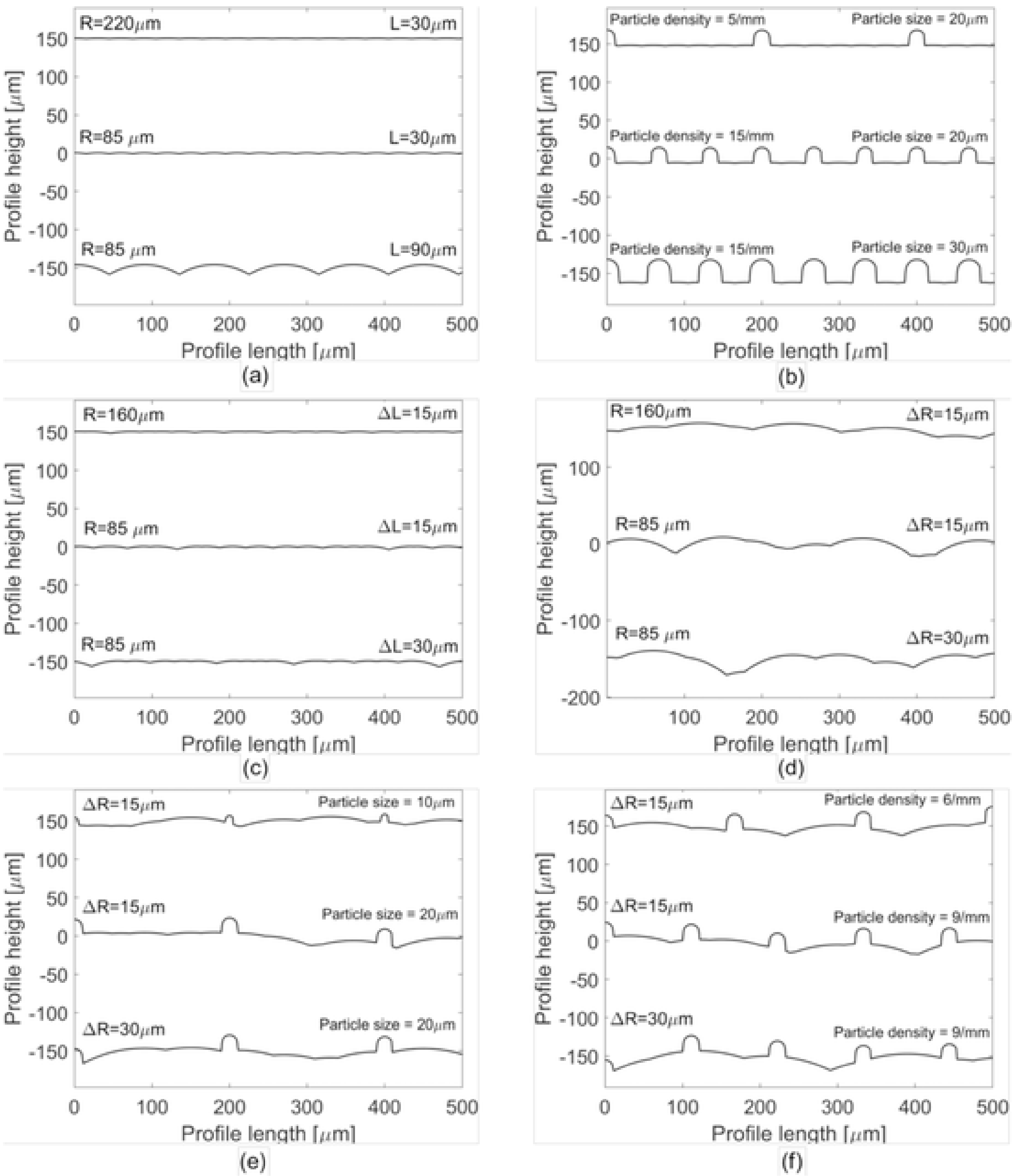

Fig. 8. Profiles generated by the model where R = melt-pool radius, L = thickness layer, ΔR = errors on R, ΔL = errors on L. (a) Ideal cases and (b) ideal cases with sintered particles with R = 160 μm. Realistic cases with (c) ΔL only varying and two different R, (d) ΔR only vary and two different R, with L = 30 μm, (e) ΔR + particles (5/mm) with R = 160 μm and L = 30 μm, (f) ΔR + particles (20 μm) with R = 160 μm and L = 30 μm.

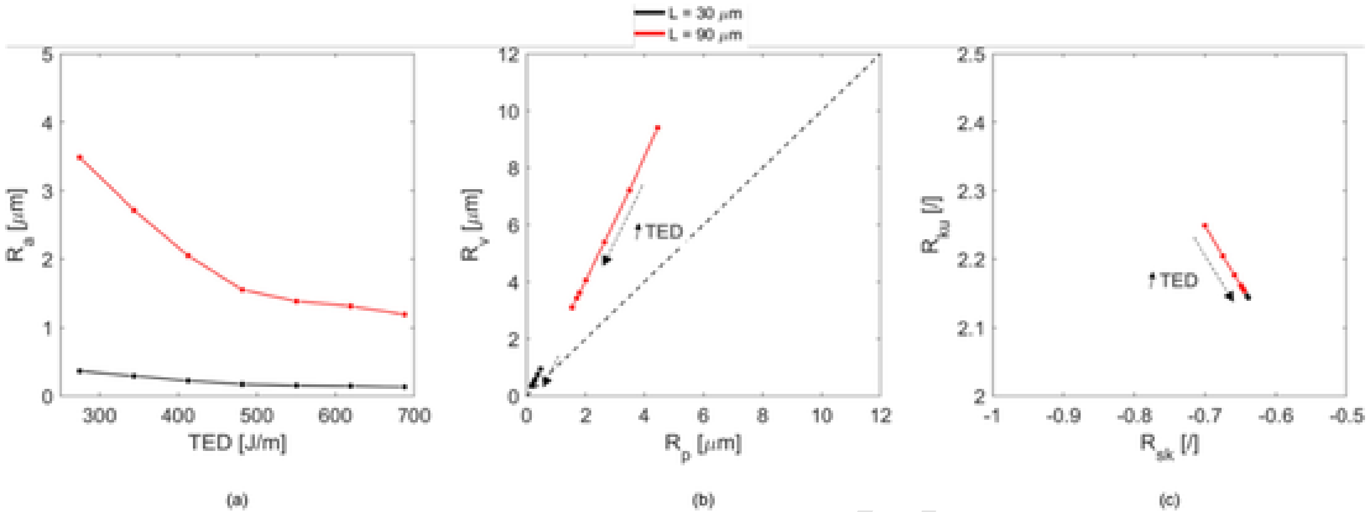

Fig. 9. Effect of TED for two different layer thicknesses, in ideal case. Arrows in R_p/R_v and R_{sk}/R_{ku} maps follow the increasing TED.

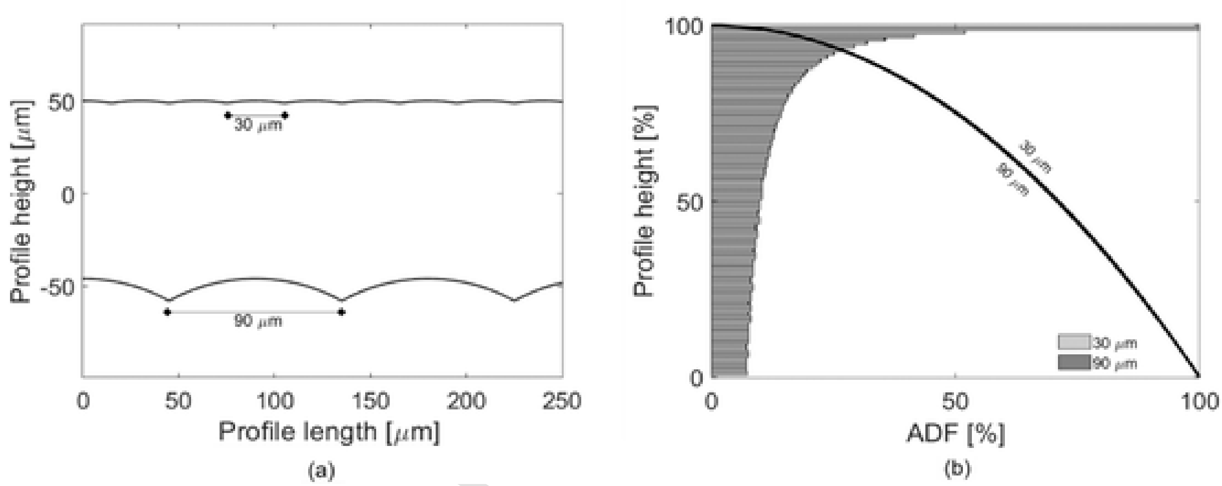

Fig. 10. Two ideal profiles (a) and their respective ADF and Abbott-Firestone curves (b). R = 160 µm. Abbott-Firestone curves and ADF of both cases overlap.

the effect becomes significant with 20 and 30 µm particles. As a reference, most commercial powders fall within the 10–60 µm range.

The R_p-R_v map reveals that adding sintered particles shifts surface profiles from valley-type to peak-type (Fig. 11b). However, beyond a critical sintered particle density, the particles are so closely packed that they form valleys instead of peaks (see Fig. 8b for a density of 15/mm and 30 µm particles). At this point, R_a reaches a maximum and then starts decreasing as sintered particle density increases further (Fig. 11a). While larger particle sizes significantly increase R_p, they have little effect on R_v—except at very high densities. Conversely, increasing particle density moves R_p closer to the $R_p = R_v$ line. This is due to the reduced spacing between particles, which decreases primary roughness and results in surface profiles primarily shaped by the sintered particles themselves, ultimately forming a valley-type profile (Fig. 11b, last point at 24 mm^{-1}). This transition corresponds to the R_a peak in Fig. 11a or the point where R_{sk} turns negative (Fig. 11c).

When sintered particles are present, R_{sk} remains positive—confirming peak-type profiles—but decreases as particle density increases (Fig. 11c). As discussed above, when the particle density becomes too high, profiles transition from peak-type ($R_{sk} > 0$) to valley-type ($R_{sk} < 0$). In all cases, R_{ku} initially spikes with the addition of a small amount of sintered powder on the flat background. This is due to the huge difference between profile height brings by the sintered particles and the primary roughness. R_{ku} is a great indicator to highlight profile “anomaly”. This can also be seen through the highly irregular Abbott-Firestone curves and ADF distributions in these conditions (Fig. 12).

Indeed, amplitude distribution functions (ADF) clearly highlight two distinct roughness contributions: the primary one from melt-pool stratification and the secondary one from sintered particles. Both contributions are also well identified in the Abbott-Firestone curves (the kink in the curves). At a density of 4/mm, the height distribution along the ADF axis is highly inhomogeneous (Fig. 12b), with particles generating extreme profile heights compared to the primary roughness (background). Since these peaks remain isolated, their proportion relative to the background is low, resulting in a high R_{ku}, which is sensitive to extreme values. Indeed, although particles represent only a small fraction of the ADF, they are the primary contributors to the profile height (Fig. 12b). As particle size or density increases, the contrast between these two contributions diminishes. At 12/mm, the elevated regions associated with particles become more frequent, and the height distribution between particles and background is more balanced, leading to a lower

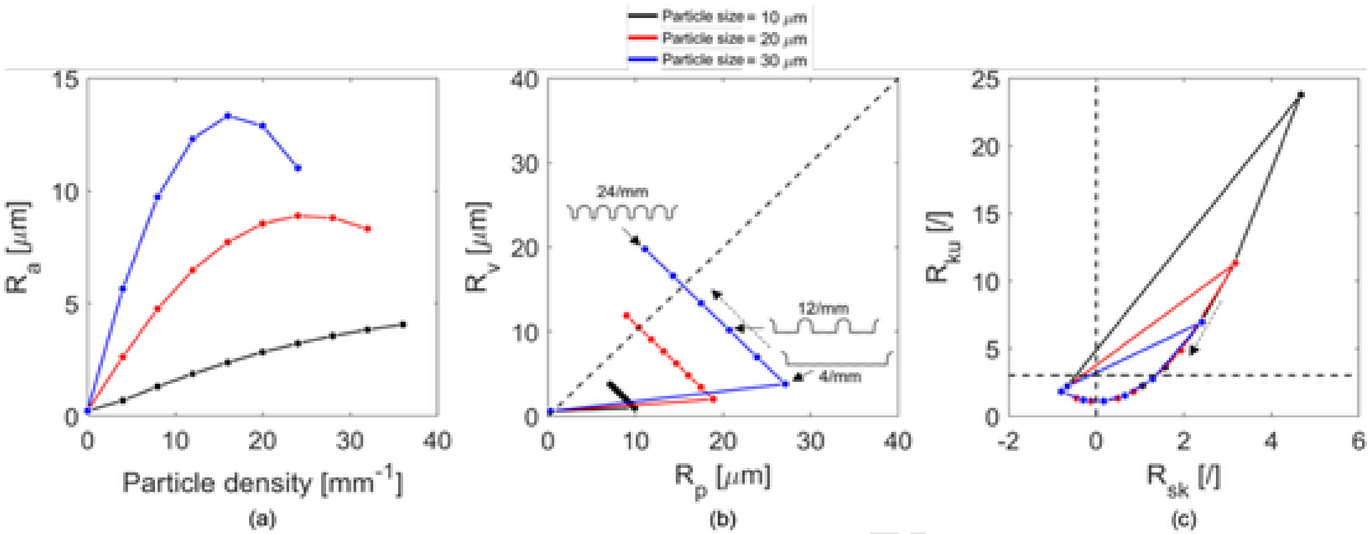

Fig. 11. Effect of particle size and density on ideal profiles. R = 160 μm and L = 30 μm. Dashed arrows indicate the increasing particle density.

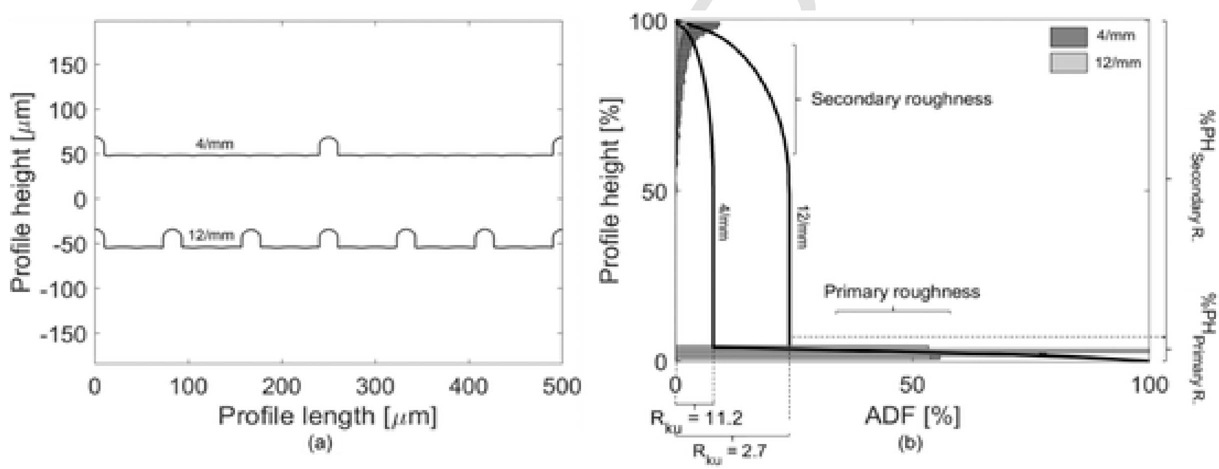

Fig. 12. Ideal profiles with particles of 20 μm (a) and their respective ADF and Abbott-Firestone curves (b). R = 160 μm and L = 30 μm. PH = profile height.

R_{ku}. The addition of sintered particles on a smooth surface significantly impacts amplitude parameters, particularly R_{sk} and R_{ku}, by altering the overall height distribution.

5.2. Realistic cases

5.2.1. Effect of layer thickness variation

Fig. 12 shows how roughness parameters change by adding an error (ΔL) on the thickness layer (L), for two melt-pool sizes. The layer thickness is set at 30 μm. The impact of ΔL is rather small. R_a slightly increases by increasing ΔL but remains below 2 μm in the worst case. Fig. 8c indeed shows that the profiles are rather flat, whatever the parameters (R or ΔL). ΔL does not have an impact on R_p but greatly increases R_v. Fig. 13a indeed show that increasing ΔL increase the size of the valley between two melt-pool. R_{sk} becomes more negative as the valley-like characteristic is accentuated. ADF and Abbott-Firestone curves clearly show that the material is mostly distributed on the top of the profile height. R_{ku} increases a lot because an increasing ΔL leads to an excessive concentration of material at the top of the profile, as shown by the ADF (Fig. 13b). Indeed, a ΔL = 60 μm induces that 3% of the highest profile heights contribute to 50% of the total distribution. The irregular spacing between melt pools become thus sharper and deeper valleys, increasing R_{ku} (Fig. 14, ΔL = 10 μm vs ΔL = 60 μm).

5.2.2. Effect of melt-pool size variation

Fig. 15 illustrates the effect of melt-pool radius variation (ΔR) on roughness parameters. The trends observed for ΔR follow the same pattern as those for ΔL, indicating a similar influence of both parameters. However, R_a increases more rapidly with ΔR than with ΔL. This is evident in Fig. 8c and d, which depict similar profile types, though those associated with ΔR exhibit a rougher and more irregular texture compared to those with ΔL.

R_v increases with ΔR more rapidly than R_p, as the valleys between melt pools deepen (Fig. 15b). Consequently, R_{sk} remains negative, indicating that most of the material lies above the profile mean line. R_{ku} also increases with ΔR but remains close to 3 (Fig. 15c), which is characteristic of a normal distribution. Indeed, the ADF tends to become more normally distributed over the profile height, as illustrated in Fig. 16 for ΔR = 15 μm. This suggests that increasing ΔR leads to a more homogeneous material distribution across the profile height.

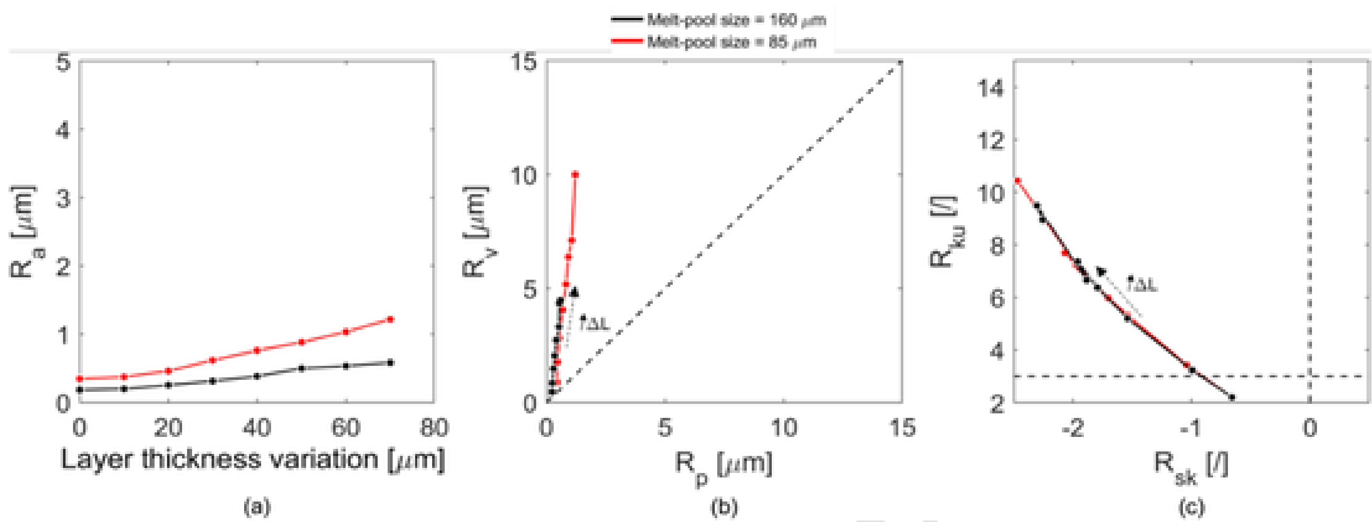

Fig. 13. Effect of ΔL (layer thickness variation) on roughness, for two melt-pool sizes. L = 30 μm and ΔR = 0. Arrows indicate an increasing ΔL.

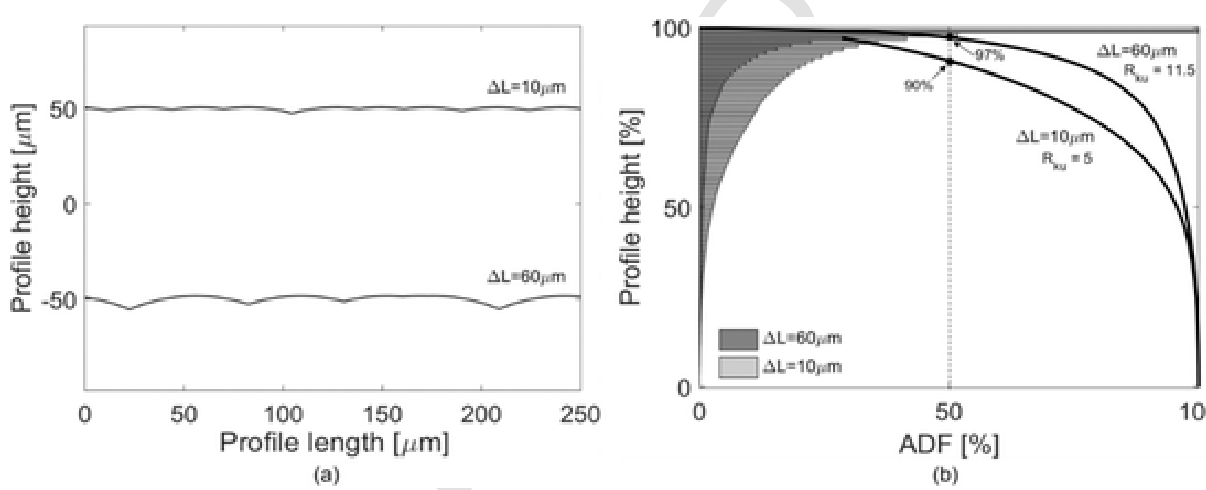

Fig. 14. Profiles with two ΔL (a) and their respective ADF and Abbott-Firestone curves (b). R = 85 μm, L = 30 μm and ΔR = 0. 3% and 10% of the highest profile heights contribute to 50% of the total height distribution for ΔL = 60 and 10 μm, respectively.

These findings also highlight that melt-pool instabilities can significantly increase surface roughness, as ΔR can become substantial in cases of the phenomenon knows as balling. Notably, the overall melt-pool size (2R) does not have a significant impact in this context, as roughness is similar between an 85 and a 160 μm-radius (Fig. 13).

5.2.3. Effect of melt-pool size variation and sintered particles

As ΔL has a marginal effect on R_a, only ΔR will be studied here. Fig. 17 illustrates the effect of adding sintered particles to the previous results for three different particle sizes (10, 20, and 30 μm) at a density of 5/mm. Compared to the particle-free case, a shift toward higher R_a values is observed, proportional to particle size (Fig. 17a). The R_p–R_v curve also shifts toward higher R_p values while maintaining the same overall trend (Fig. 17b). This confirms that the addition of powder primarily increases R_p, whereas errors on the radius (ΔR) mainly affect R_v. Notably, the increase in R_p appears to scale with particle size.

As in the ideal case with particle density (Fig. 11c), for low ΔR, the R_{sk}–R_{ku} curves start in the upper-right quadrant ($R_{sk} > 0$ and $R_{ku} > 3$). Fig. 18 presents the ADF for three different ΔR (circled points in Fig. 16). $R_{sk} > 0$ as most of the profile heights lie below the mean line for the three ΔR. For example, at ΔR = 5 μm, only 31% of the profile heights are above the mean line. At low ΔR, the primary roughness is very smooth, making particle-induced peaks stand out as extreme values, leading to a high R_{ku}. A rougher primary roughness, due to higher ΔR, reduces the contrast between particles and the underlying surface, lowering R_{ku}. With an even higher ΔR, particles blend into the overall distribution, further decreasing R_{ku}, as the ADF shape is close to a Gaussian distribution, i.e., $R_{sk} = 0$ and $R_{ku} = 3$ (Fig. 18c). The particle size has a minor impact on R_{sk}–R_{ku}, only slightly reducing the slope of the curves. R_{sk} increase with particle size as it increases the peakedness of the profiles.

Fig. 19 presents the effect of the particle density. The effect of increasing particle density is similar to that of increasing particle size, although its impact on the R_p and R_v indicators appears more limited (Fig. 19b). In particular, R_p seems to be governed more by particle size than by their density. The effect on R_{sk} and R_{ku} is similar because increasing particle size or increasing particle density have the same effect on ADF: the contribution of the secondary roughness increases.

For all profiles generated in this study, particle positions are independent of the peak and valley locations. However, it is worth noting

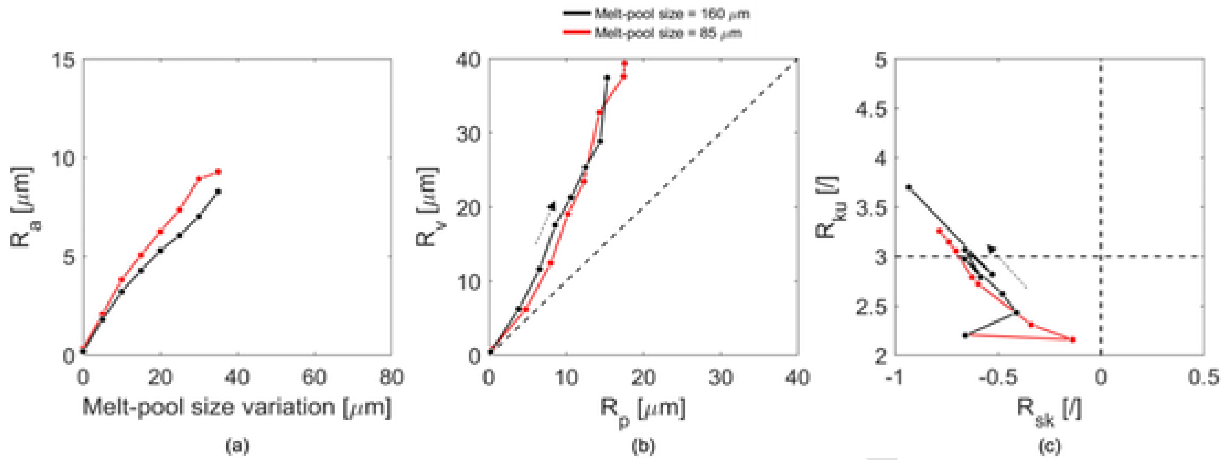

Fig. 15. Effect of ΔR on roughness for two melt-pool sizes. L = 30 μm and ΔL = 0. Arrows indicate an increasing melt-pool size variation (ΔR).

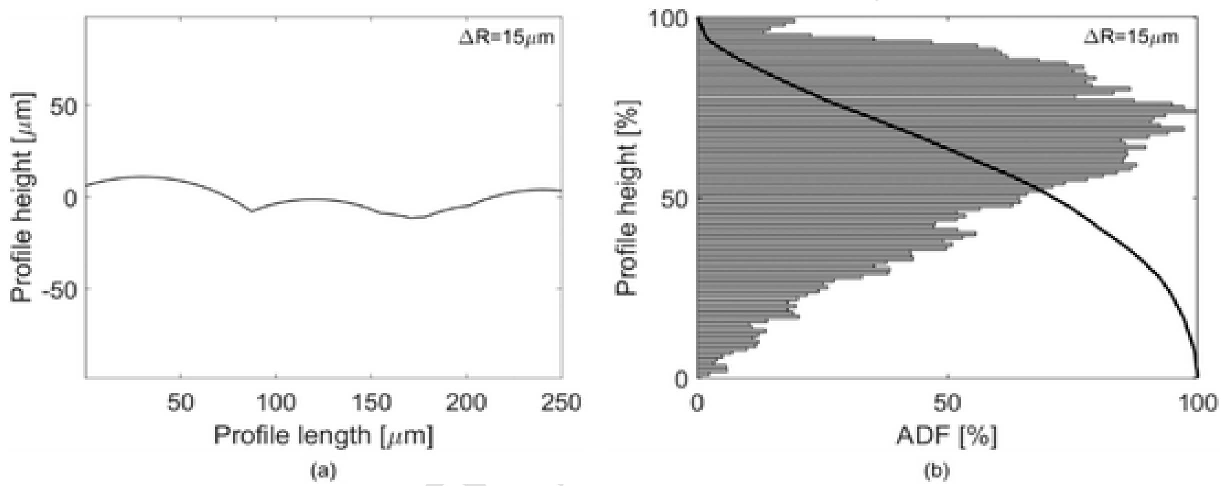

Fig. 16. Profile with ΔR and its respective ADF and Abbott-Firestone curves. R = 85 μm, L = 30 μm and ΔL = 0.

that the effect of sintered particles on R_{sk} and R_{ku} also depends on their spatial positioning. Specifically, when particles are located at either the peaks or valleys of the profile, their impact differs significantly. This effect is illustrated in Fig. 20, which presents idealized cases where particle positions are deliberately controlled. When particles are situated in the valleys, the secondary ADF merges with the primary ADF, resulting in a lower R_{ku}. Conversely, when particles are predominantly located at the peaks of the primary roughness, R_{ku} increases.

5.2.4. *All together*

Each parameter has been analyzed individually, and their effects have been clearly highlighted. Fig. 21 presents a global view of their combined influence based on experimental data, considering two levels of process instabilities (ΔR and ΔL = 10 or 20 μm), two particle sizes (10 and 20 μm), and two particle densities (5 and 10/mm), all as a function of TED. The results indicate that TED has a limited impact on roughness, although its effect can be amplified by increasing process instabilities ΔR and ΔL (dashed curves). In all cases studied here, R_a exhibits only a slight decrease with TED. Similarly, R_p and R_v are only marginally affected, except when ΔR and ΔL reach 20 μm. R_{sk} and R_{ku} show no significant variations with TED, reinforcing the idea that TED plays a secondary role in this context.

Conversely, addition of sintered particle has a pronounced impact on roughness. Introducing 10 μm particles has little effect on R_a but significantly increases R_p, roughly in proportion to the particle size (red curves in Fig. 21). Adding 20 μm particles leads to a rise in R_a and a further increase in R_p, while R_v remains unaffected (blue curves in Fig. 21). This behaviour is consistent with the ideal case (Fig. 11) and with scenarios involving only ΔR (Fig. 17). Furthermore, the presence of sintered particles increases both R_{sk} and R_{ku}, shifting them from the lower-left to the upper-right quadrant (Fig. 21c).

Increasing particle density influences R_a to the same extent as increasing particle size but has a lesser effect on R_p and R_v, causing only a minor shift toward the $R_p = R_v$ axis (green curves in Fig. 21). It also raises R_{sk} by enhancing secondary roughness contributions while slightly decreasing R_{ku} due to improved ADF homogeneity, as observed in Section 5.2.3.

Higher ΔR and ΔL values lead to an increase in R_a (dashed curves in Fig. 21). For both particle sizes, they have a more significant effect on R_v than on R_p, shifting the curves toward the $R_p = R_v$ axis. In the R_{sk}/R_{ku} plot, increasing ΔR and ΔL shifts the curves back toward the lower-left quadrant, i.e., toward nearly Gaussian profile height distributions.

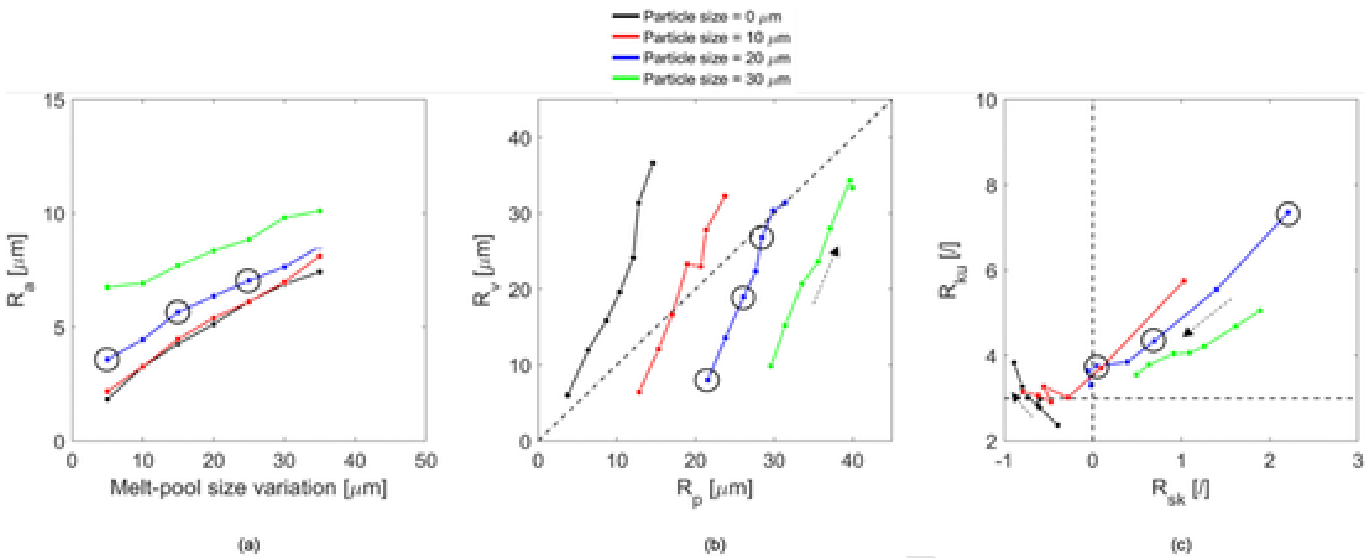

Fig. 17. Effect of melt-pool size variation with different particle sizes on roughness. The density of particle is 5/mm. R = 160 μm, L = 30 μm and ΔL = 0. Arrows indicate the increasing ΔR. ADF of circled points are exhibited in Fig. 18.

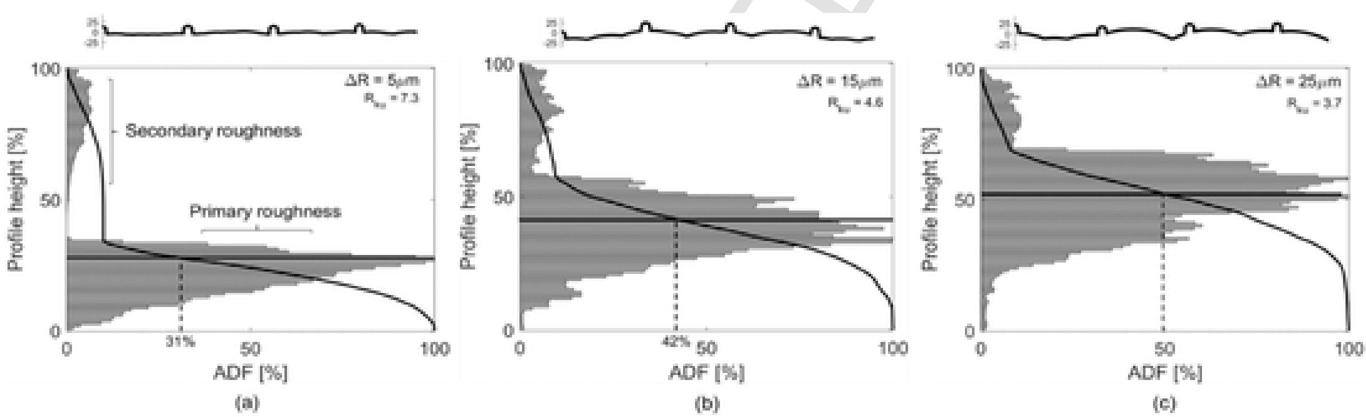

Fig. 18. Effects of ΔR with particle density of 5/mm and particle size of 20 μm on ADF and Abbott-Firestone curves. R = 160 μm, L = 30 μm and ΔL = 0.The black horizontal lines are mean line of the respective profiles.

It is also worth noticing that a same level of R_a (black and red curves, for example), can have different causes, as R_p/R_v and R_{sk}/R_{ku} are different.

6. Discussion

The effects of each parameter studied in this work on profiles are illustrated in Fig. 22, using a small R to better highlight them. Increasing L extends the remaining side portion of each melt pool, enhancing the valley-like nature of the profiles due to the layer-by-layer nature of the process. Similarly, decreasing R intensifies this effect by increasing the curvature of each melt pool. Unsurprisingly, the addition of particles significantly increases roughness by contributing to profile height. The effect of ΔL on profile height is relatively limited, resulting in only a slight influence on roughness. Conversely, ΔR directly affects profile height, especially when particles are present, leading to a substantial increase in roughness.

As previously demonstrated, roughness can be decomposed into two main components: primary roughness, which arises from the melt-pool geometry and the inherent layer-by-layer structure of the process, and secondary roughness, caused by sintered particles on the profile surface. It is important to note that, in this study, the increase in melt-pool size and the onset of instabilities due to TED are considered separately to isolate their effects, even though they are naturally correlated in practice.

From a physical standpoint, melt-pool size is controlled by TED. Geometrically, increasing TED reduces primary roughness by decreasing the residual curvature on the sides of the melt pool, as guessed in [1]. However, the model results clearly indicate that TED has a very limited effect on overall roughness and therefore cannot account for the experimentally observed decrease in R_a (Fig. 7). In contrast, melt-pool instabilities (ΔR) and sintered particles have a significant impact on roughness by substantially increasing profile height (Fig. 22).

In particular, the presence of sintered surface particles significantly increases both R_a and R_p values.

This has been confirmed experimentally, as recent studies have highlighted the strong influence of powder distribution on side surface roughness [45]. The parameter R_a alone is not a reliable indicator for understanding roughness, as different combinations of R_p and R_v can result in the same R_a value. The present results therefore emphasize that

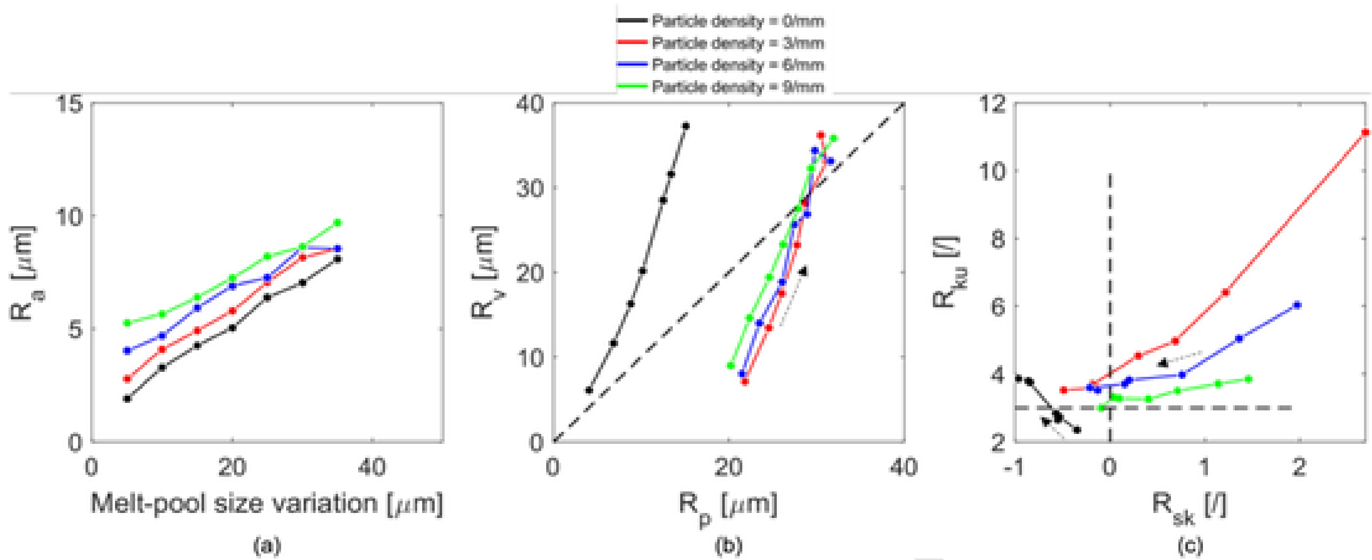

Fig. 19. Effect of melt-pool size variation with different particle density on roughness. The size of particles is 20 μm. R = 160 μm, L = 30 μm and ΔL = 0. Arrows indicate the increasing ΔR.

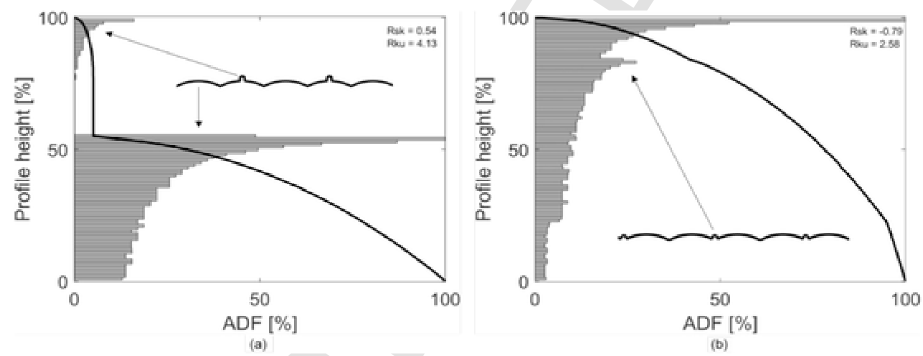

Fig. 20. Effect of particle positioning on ADF. Particles are positioned on (a) the top of the peaks and (b) at the bottom of the valleys. R = 90 μm, L = 90 μm, ΔR and ΔL = 0, particle density = 5/mm and particle size = 10 μm.

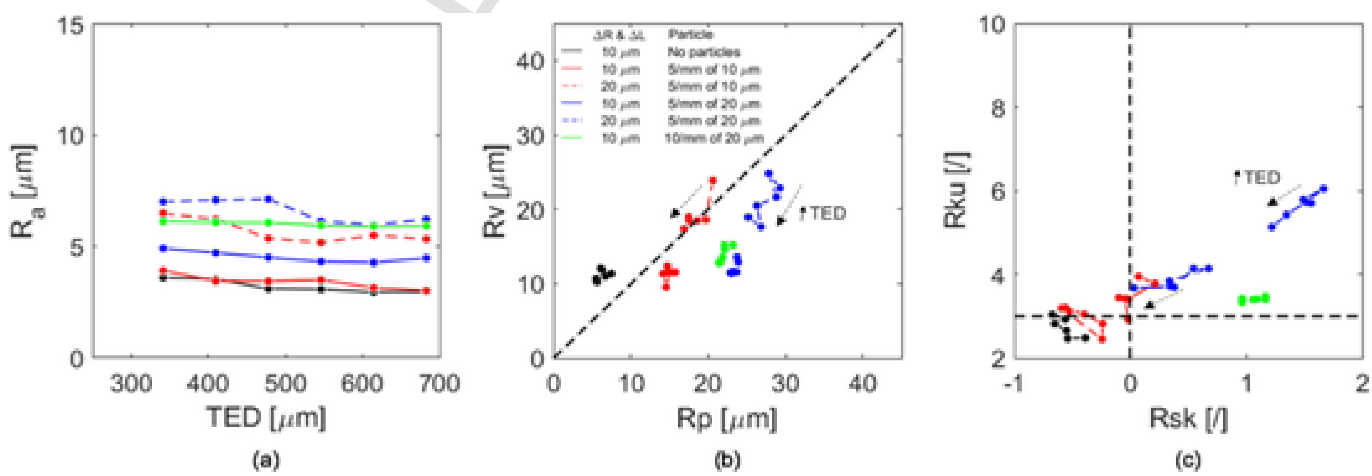

Fig. 21. Effect of melt-pool size and thickness layer variation and TED together with different particle density on roughness. The size of particles is 20 μm. L = 30 μm. Arrows indicate an increasing TED.

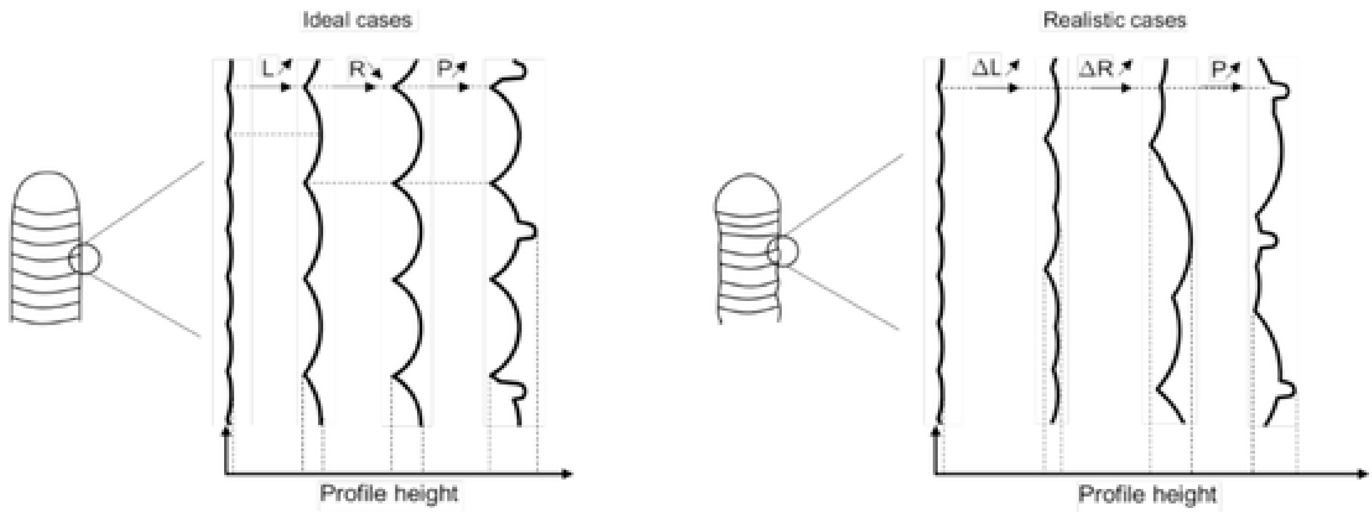

Fig. 22. Summering the effects of each parameter on profile shape and height. L = thickness layer. R = melt-pool radius. P = particle density.

surface optimization strategies should not rely solely on R_a, but rather consider how different surface features affect the full set of roughness parameters. While reducing R_a is a reasonable objective for minimizing roughness amplitude, the analysis shows that R_p and R_v provide complementary information on the relative contributions of peaks and valleys to the surface profile. It is worth noting that, even though particles tend to generate peak-like surface profiles, the underlying primary roughness remains valley-dominated. This explains the generally poor fatigue performance of as-built L-PBF AlSi10Mg parts, as surface valleys act as stress concentrators and promote early failure [11,12].

The results also indicate that R_{sk} and R_{ku} depend on the interplay between primary and secondary roughness. For instance, a small number of particles on an otherwise smooth surface results in a high R_{ku} and a positive R_{sk}, as the associated ADF is highly inhomogeneous. Increasing instabilities (ΔR and ΔL) causes the ADF of the particles to merge with that of the primary roughness, thereby reducing R_{ku}. However, particle positioning also plays a role. If, for physical reasons, particles preferentially accumulate in valleys (Fig. 20), their ADF signature blends with the primary roughness ADF, maintaining a low R_{ku}. More generally, surfaces approaching $R_{sk} \approx 0$ and $R_{ku} \approx 3$ correspond to height distributions closer to a Gaussian profile, which typically reflects a more homogeneous surface morphology. Slightly negative R_{sk} values may even be preferable in some cases, as valley-dominated surfaces reduce the presence of isolated peaks that may act as critical stress concentrators.

7. Conclusion

Roughness in LPBF-manufactured parts remains a critical challenge in additive manufacturing, with complex dependencies on process parameters that are not always well understood. To address this, a geometry-based model was developed, capable of capturing the key effects of parameters such as TED, layer thickness, and sintered particle size on surface roughness. The model was calibrated by experimental data, allowing for a deeper analysis of roughness formation mechanisms beyond the commonly used R_a parameter.

This study highlights the need to distinguish between primary roughness, which originates from melt-pool geometry, and secondary roughness, which results from sintered particles. It was demonstrated that TED mostly influences primary roughness but has a limited impact on overall roughness. In contrast, instabilities (ΔR) and sintered particles play a dominant role by significantly increasing profile height. Furthermore, our analysis shows that R_p and R_v provide a more precise characterization of roughness than R_a alone, as they directly correlate with the underlying mechanisms. Additionally, the parameters R_{sk} and R_{ku} were found to depend on the interplay between primary and secondary roughness, with particle distribution influencing their values.

Overall, this work underscores the limitations of relying solely on R_a and emphasizes the importance of a multi-parameter approach for characterizing and controlling roughness in LPBF. The insights gained from this model provide a foundation for optimizing process parameters to achieve improved surface quality in additive manufacturing.

More advanced signal decomposition techniques (Fourier Transform, machine learning, etc.) would possibly allow a more compact mathematical representation of the profile. However, such approaches would reduce the direct physical interpretability of the descriptors and would not have the physical benefits of the step by step approach of the present simple model.

CRediT authorship contribution statement

Olivier Poncelet: Writing – review & editing, Writing – original draft, Visualization, Validation, Supervision, Project administration, Methodology, Investigation, Funding acquisition, Formal analysis, Data curation, Conceptualization. **Camille van der Rest:** Writing – review & editing, Methodology, Formal analysis, Conceptualization. **Aude Simar:** Writing – review & editing, Supervision, Resources, Funding acquisition.

Declaration of Generative AI and AI-assisted technologies in the writing process

During the preparation of this work the author(s) used Chatgpt in order to improve language and readability. After using this tool/service, the author(s) reviewed and edited the content as needed and take (s) full responsibility for the content of the publication.

Declaration of competing interest

The authors declare that they have no known competing financial interests or personal relationships that could have appeared to influence the work reported in this paper.

Acknowledgment

The present work was supported by the Walloon Region through the WINGS (Walloon Innovation for Green Skies) project (RW 8441) and the win2wal 2025 project ThinWaAl. This work has been performed with the help of the Lacami technological platform of UCLouvain.

References

[1] Poncelet Olivier, Marteleur Matthieu, van der Rest Camille, Rigo O, Adrien J, Dancette Sylvain, et al. Critical assessment of the impact of process parameters on vertical roughness and hardness of thin walls of AlSi10Mg processed by laser powder bed fusion. Addit Manuf 2021;38.

[2] Aboulkhair Nesma T, Maskery lan, Tuck Chris, Ashcroft lan, Everitt Nicola M. Improving the fatigue behaviour of a selectively laser melted aluminium alloy: influence of heat treatment and surface quality. Mater Des 2016;104.

[3] Greitemeier D, Dalle Donne C, Syassen F, Eufinger J, Melz T. Effect of surface roughness on fatigue performance of additive manufactured Ti6Al4V. Mater Sci Technol 2016;32:7.

[4] Brandao Ana D, Gumpinger Johannes, Gschweitl Michael, Seyfert Christoph, Hofbauer Peter, Ghidini Tommaso. Fatigue properties of additively manufactured AISi10Mg — surface treatment effect. Procedia Struct Integrity 2017;7.

[5] Lv Zhao, Juan Guillermo Santos Macias, Lipeng Ding, Hosni Idrissi, Aude Simar. Damage mechanisms in selective laser melted AlSi10Mg under as built and different post-treatment conditions. Mater Sci Eng A 2019;764.

[6] Hamidi Nasab Milad, Giussani Alessandro, Gastaldi Dario, Tirelli Valeria, Vedani Maurizio. Effect of surface and subsurface defects on fatigue behavior of AlSi10Mg alloy processed by laser powder bed fusion (L-PBF). Metals 2019;9(10).

[7] Nicoletto Gianni. Influence of rough as-built surfaces on smooth and notched fatigue behavior of L-PBF AlSi10Mg. Addit Manuf 2020;34.

[8] Du Plessis A, Beretta S. Killer notches: the effect of as-built surface roughness on fatigue failure in AlSi10Mg produced by laser powder bed fusion. Addit Manuf 2020;35.

[9] Masiagutova E, Cabanettes F, Sova A, Cici M, Bidron G, Bertrand P. Side surface topography generation during laser powder bed fusion of AlSi10Mg. Addit Manuf 2021;47:102230.

[10] Seabra Miguel, Azevedo José, Araujo Aurélio, Reis Luis, Pinto Elodie, Alves Nuno, et al. Selective laser melting (SLM) and topology optimization for lighter aerospace components. Procedia Struct Integrity 2016;1.

[11] Cheng Zhengkun, Liao Ridong, Lu Wei. Surface stress concentration factor via Fourier representation and its application for machined surfaces. Int J Solids Struct 2017;113:108–17.

[12] van der Rest Camille, Navarrete Rodrigo Arturo Manzano, Simar Aude, Poncelet Olivier. Influence of roughness and subsurface porosity on the fatigue life of AlSi10Mg produced by Laser Powder Bed Fusion. Mater Sci Eng A 2025;148885.

[13] Calignano Flaviana. Investigation of the accuracy and roughness in the laser powder bed fusion process. Virtual Phys Prototyp 2018;13:2.

[14] Calignano Flaviana, Peverini Oscar Antonio, Addamo Giuseppe, Iuliano Luca. Accuracy of complex internal channels produced by laser powder bed fusion process. J Manuf Process 2020;54.

[15] Pyka Grzegorz, Kerckhofs Greet, Papantoniou loannis, Speirs Mathew, Schrooten Jan, Wevers Martine. Surface roughness and morphology customization of additive manufactured open porous Ti6AI4V structures. Materials 2013;6(10).

[16] Delroisse Pauline, Jacques Pascal J, Maire Eric, Rigo Olivier, Simar Aude. Effect of strut orientation on the microstructure heterogeneities in AlSi10Mg lattices processed by selective laser melting. Scr Mater 2017;141:32–5.

[17] Han Xuesong, Zhu Haihong, Nie Xiaojia, Wang Guoging, Zeng Xiaoyan. Investigation on selective laser melting AISILOMg cellular lattice strut: molten pool morphology, surface roughness and dimensional accuracy. Materials 2018;11:3.

[18] Yang Tao, Liu Tingting, Liao Wenhe, MacDonald Eric, Wei Huiliang, Chen Xiangyuan, et al. The influence of process parameters on vertical surface roughness of the AISi10Mg parts fabricated by selective laser melting. J Mater Process Technol 2019;266.

[19] Gouveia Ronny M, Silva Francisco JG, Atzeni Eleonora, Sormaz Dufvsan, Alves Jorge Lino, Pereira Antonio Bastos. Effect of scan strategies and use of support structures on surface quality and hardness of L-PBF AISi10Mg parts. Materials 2020;13:10.

[20] Cabanettes Frédéric, Joubert A, Chardon G, Dumas V, Rech J, Grosjean C, et al. Topography of as built surfaces generated in metal additive manufacturing: a multi scale analysis from form to roughness. Precis Eng 2018;52.

[21] Strano Giovanni, Hao Liang, Everson Richard M, Evans Kenneth E. Surface roughness analysis, modelling and prediction in selective laser melting. J Mater Process Technol 2013;213:4.

[22] Hitzler Leonhard, Hirsch Johann, Merkel Markus, Ochsner Andreas. Thermal environment and inclination angle dependencies on the surface quality of selective laser melted 316L steel. Defect Diffusion Forum 2016;372:202–7.

[23] DePond Philip J, Guss Gabe, Ly Sonny, Calta Nicholas P, Deane Dave, Khairallah Saad, et al. In situ measurements of layer roughness during laser powder bed fusion additive manufacturing using low coherence scanning interferometry. Mater Des 2018;154.

[24] Whip Bo, Sheridan Luke, Gockel Joy. The effect of primary processing parameters on surface roughness in laser powder bed additive manufacturing. Int J Adv Manuf Technol 2019;103(9–12):4411–22.

[25] Roti Sebastian, Ladewig Alexander, Friedberger Katrin, Casper Johannes, Full Moritz, Schleifenbaum Johannes Henrich. Surface roughness in laser powder bed fusion — interdependency of surface orientation and laser incidence. Addit Manuf 2020;36.

[26] Balbaa Mohamed, Mekhiel Sameh, Elbestawi Mohamed, Mclsaac Jeff. On selective laser melting of Inconel 718: densification, surface roughness, and residual stresses. Mater Des 2020;193.

[27] Townsend Andrew, Senin N, Blunt Liam, Leach RK, Taylor JS. Surface texture metrology for metal additive manufacturing: a review. Precis Eng 2016;46.

[28] Bigerelle Maxence, Najjar Denis, Mathia Thomas, lost Alain, Coorevits Thierry, Anselme Karine. An expert system to characterise the surfaces morphological properties according to their tribological! functionalities: the relevance of a pair of roughness parameters. Tribol Int 2013;59:190–202.

[29] Horvath Richard, Czifra Arpad, Dregelyi-Kiss Agota. Effect of conventional and non-conventional tool geometries to skewness and kurtosis of surface roughness in case of fine turning of aluminium alloys with diamond tools. Int J Adv Manuf Technol 2015;78(1–4):297–304.

[30] Krolczyk GM, Krolczyk JB, Maruda RW, Legutko S, Tomaszewski M. Metrological changes in surface morphology of high-strength steels in manufacturing processes. Measurement 2016;88:176–85.

[31] Boschetto Alberto, Bottini Luana, Veniali Francesco. Roughness modeling of AlSi10Mg parts fabricated by selective laser melting. J Mater Process Technol 2017;241.

[32] Yu Guanqun, Gu Dongdong, Dai Donghua, Xia Mujian, Ma Chenglong, Shi Qimin. On the role of processing parameters in thermal behavior, surface morphology and accuracy during laser 3D printing of aluminum alloy. J Phys D Appl Phys 2016;49:13.

[33] Yadroitsev, Gusarov A, Yadroitsava, Smurov. Single track formation in selective laser melting of metal powders. J Mater Process Technol 2010;210(12).

[34] Zheng Min, Wei Lei, Chen Jing, Zhang Qiang, Zhong Chongliang, Lin Xin, et al. A novel method for the molten pool and porosity formation modelling in selective laser melting. Int J Heat Mass Transf 2019;140.

[35] King Wayne E, Barth Holly D, Castillo Victor M, Gallegos Gilbert F, Gibbs John W, Hahn Douglas E, et al. Observation of keyhole-mode laser melting in laser powder-bed fusion additive manufacturing. J Mater Process Technol 2014;214(12):2915–25.

[36] Dai Donghua, Gu Dongdong. Effect of metal vaporization behavior on keyhole-mode surface morphology of selective laser melted composites using different protective atmospheres. Appl Surf Sci 2015;355:310–9.

[37] Kempen Karolien, Thijs Lore, Van Humbeeck Jan, Kruth J-P. Processing AlSi10Mg by selective laser melting: parameter optimisation and material characterisation. Mater Sci Technol 2015;31(8):917–23.

[38] Gheysen Julie, Marteleur Matthieu, van der Rest Camille, Simar Aude. Efficient optimization methodology for laser powder bed fusion parameters to manufacture dense and mechanically sound parts validated on AlSi12 alloy. Mater Des 2021;199:109433.

[39] Ali Usman, Esmaellizadeh Reza, Ahmed Farid, Sarker Dyuti, Muhammad Wagqas, Keshavarzkermani Aliand, et al. Identification and characterization of spatter particles and their effect on surface roughness, density and mechanical response of 17-4 PH stainless steel laser powder-bed fusion parts. Mater Sci Eng A 2019;756:98–107.

[40] Rosenthal D. Mathematical theory of heat distribution during welding and cutting. Weld J 1941;20:220–34.

[41] Tang M, Pistorius PC, Beuth JL. Prediction of lack-of-fusion porosity for powder bed fusion. Addit Manuf 2017;14:39–48.

[42] Tang M, Pistorius PC, Narra S, Beuth JL. Rapid solidification: selective laser melting of AlSi10Mg. Jom 2016;68(3):960–6.

[43] Moda Mattia, Chiocca Andrea, Macoretta Giuseppe, Monelli Bernardo Disma, Bertini Leonardo. Technological implications of the Rosenthal solution for a moving point heat source in steady state on a semi-infinite solid. Mater Des 2022;223:110991.

[44] Keeley William, Turner Richard, Mitchell Bashir, Warnken Nils. A development of the Rosenthal equation for predicting thermal profiles during additive manufacturing. Thermo 2025;5:2.

[45] Park M, Su S, Ghosh A, Muniz-Lerma JA, Espiritu ERL, Colon M, et al. Effect of particle size distribution on the sidewall surface roughness of AlSi10Mg parts manufactured by laser powder bed fusion. Results Eng 2025;105532.